

# Vortex nucleations in spinor Bose condensates under localized synthetic magnetic fields

L. -R. Liu,<sup>1</sup> S. -C. Wu,<sup>1</sup> T. -W. Liu,<sup>1</sup> H. -Y. Hsu,<sup>1</sup> T. -K. Shen,<sup>1</sup> S. -K. Yip,<sup>1,2</sup> Y. Kawaguchi,<sup>3,4</sup> and Y. -J. Lin<sup>1,5</sup>

<sup>1</sup>*Institute of Atomic and Molecular Sciences, Academia Sinica, Taipei, Taiwan 10617*

<sup>2</sup>*Institute of Physics, Academia Sinica, Taipei, Taiwan 11529*

<sup>3</sup>*Department of Applied Physics, Nagoya University, Nagoya, 464-8603, Japan*

<sup>4</sup>*Research Center for Crystalline Materials Engineering, Nagoya University, Nagoya 464-8603, Japan*

<sup>5</sup>*Department of Physics, National Tsing Hua University, Hsinchu 30013, Taiwan*

(Dated: March 27, 2024)

Gauge fields are ubiquitous in modern quantum physics. In superfluids, quantized vortices can be induced by gauge fields. Here we demonstrate the first experimental observation of vortex nucleations in spinor Bose-Einstein Condensates under radially-localized synthetic magnetic fields. The associated gauge potentials  $\vec{A}$  are azimuthal and created by light-induced spin-orbital-angular-momentum coupling, generating circulating azimuthal velocity fields  $\propto \vec{p} - \vec{A}$  even when the canonical momentum  $\vec{p} = 0$ . A sufficiently large azimuthal velocity peaked near the condensate center results in a dynamically unstable localized excitation that initiates vortex nucleations. This excitation appears as a spontaneously-formed vortex-antivortex pair near the cloud center. Following the initially developed instability, the dynamics is governed by the asymmetry and dissipation, where the atomic orbital angular momentum evolves and can reach the value of the ground state. Our system exhibits dynamical and Landau instabilities and agrees reasonably with time-dependent Gross-Pitaevskii simulations.

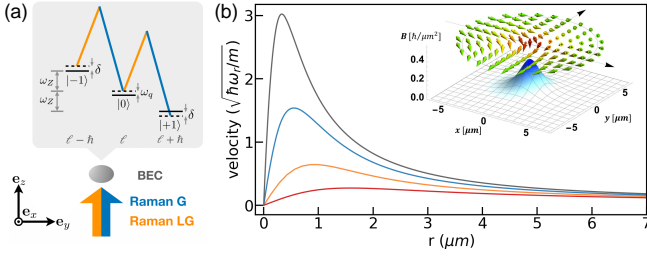
The realization of synthetic gauge fields for charge-neutral ultracold atoms has opened new opportunities for creating and investigating topological quantum matters in a clean and easy-to-manipulate environment [1–4]. Early pioneering experiments utilize mechanical rotation to create an effective Lorentz force and thus effective magnetic fields in the rotating frame [5–8], however, some technical issues pose limitations to such mechanical rotation methods [9–11]. Further, mechanical rotations create only a uniform effective magnetic field  $B^*$  with a synthetic gauge potential restricted to the symmetric gauge along the azimuthal direction,  $\vec{A} = B^*(-y\mathbf{e}_x + x\mathbf{e}_y)/2$ . A breakthrough was achieved by the realization of laser-engineered synthetic gauge potentials, which enabled us to implement the Landau gauge  $\vec{A} = -B^*y\mathbf{e}_x$  [12] and engineer more versatile and general forms of  $\vec{A}$ . Such laser-engineered  $\vec{A}$  appears in the laboratory frame with a stationary Hamiltonian and may circumvent the technical issues in mechanically rotating systems. This paves the way towards inducing rotation of normal atoms and thus measuring superfluid fractions [13], and reaching the fast-rotation regime and quantum-Hall states.

Under such a variety of synthetic gauge fields, a question naturally arises as to how vortices are nucleated. In the case of mechanical rotation, quantized vortices have attracted extensive studies, which also appear in other systems such as helium superfluids, superconductors and neutron stars. Such quantized circulation and the corresponding irrotational flow originate from a single-valued superfluid order parameter. Vortex nucleations are of particular interest as they manifest transitions between different topological states. In atomic quantum gases, early works investigated vortex nucleations in mechan-

ically stirred rotating scalar Bose-Einstein condensates (BECs), including experiments [5, 7, 11, 14–16] and simulations [17–22]. When a BEC with a negligibly small amount of thermal atoms is stirred with a rotating elliptical deformation of the external trapping potential [5, 14, 15], vortices are nucleated from the edge of the BEC owing to dynamical instabilities occurring at the rotating frequency nearly resonant with that of the surface quadrupole mode. This critical frequency is significantly higher than that for thermodynamically stable single-vortex [23]. The  $2\pi$  phase slips between quantized supercurrents in ring-shaped quantum gases are also studied in Ref. [24–28].

Light-induced synthetic magnetic fields with the Landau gauge can also nucleate vortices, as studied experimentally [12, 29, 30] and theoretically [31]. Here the synthetic field arises from the coupling between the atoms' internal spin and the center-of-mass linear momentum provided by Raman laser dressing, a spin-orbit coupling. In the experiments [12, 29], vortices are observed to appear from the edge when the initial vortex-free system is thermodynamically unstable. More recently, physicists also realize synthetic magnetic fields under azimuthal gauge potentials [32–34]. This is achieved by coupling the atomic internal spin states and the center-of-mass orbital-angular-momentum (OAM), which we refer to as spin-OAM coupling.

In this Letter, we report the first experimental observation of vortex nucleation in a spinor BEC under synthetic azimuthal gauge potentials. The synthetic magnetic field  $\vec{B} = \vec{\nabla} \times \vec{A}$  is localized around  $r \sim 0$  (see Fig. 1b inset) in an almost cylindrically-symmetric system with the coordinate  $(r, \phi, z)$ . It creates a circulating kinetic velocity



field  $(\hbar\nabla\vartheta - \vec{A})/m$  in a vortex-free system with  $\vec{\nabla}\vartheta \approx 0$ , where  $m$  is the atomic mass and  $\vartheta$  is the phase of the condensate wave function. In the experiment, we adiabatically turn on the gauge field, hold the system for some time, and then adiabatically turn off the gauge field to probe the change in the profile of  $\vartheta$  via density images and OAM measurements. The azimuthal velocity under  $\vec{A}$  has a maximal value at small  $r$  (see Fig. 1b), and when it exceeds the critical velocity, a mode localized at  $r \sim 0$  has a negative energy. When this mode couples with another positive-energy excitation, dynamical instability arises and triggers vortex nucleation. The signature of this dynamical instability is observed as vortex-antivortex-pair generation near the center. The subsequent vortex nucleation proceeds with the aid of asymmetry and dissipation, essential for violating OAM and energy conservations. Although Refs. [35, 36] theoretically investigate vortex-nucleation dynamics under nonuniform synthetic magnetic fields, their  $|\vec{B}|$  and  $|\vec{A}|$  increase with  $r$  and consequently vortices enter from the edge due to the instability of surface modes. Our vortex nucleation has drastically different features from those with uniform and nonuniform [35, 36] synthetic magnetic fields.

We implement the gauge potential by loading a spin  $F = 1$   $^{87}\text{Rb}$  BEC into the lowest-energy branch of the Raman-dressed states [33], where a Gaussian Raman beam and a Laguerre-Gaussian (LG) Raman beam with phase winding 1 transfer OAM of  $\pm\hbar$  when coupling the bare spin state  $|m_F\rangle$  to  $|m_F \pm 1\rangle$  (Fig. 1a). The gauge field is controlled via the Raman detuning  $\delta = \Delta\omega_L - \omega_Z$ , with  $\Delta\omega_L$  being the frequency difference between the two Raman beams and  $\omega_Z$  the linear Zeeman shift, under a small quadratic Zeeman shift  $\omega_q/2\pi \approx 50$  Hz and a Raman coupling strength  $\Omega(r) = \Omega_M\sqrt{e}(r/r_M)e^{-r^2/2r_M^2}$  with peak coupling  $\Omega_M/2\pi = 2.5(2)$  kHz at  $r_M = 17 \mu\text{m}$ . In the dressed state, the bare spin  $|m_F = 0, \pm 1\rangle$  component has OAM  $\ell + m_F\hbar$ , where  $\ell$  is the quasi-OAM. The position-dependent spinor  $|\xi_{-1}\rangle$  corresponding to

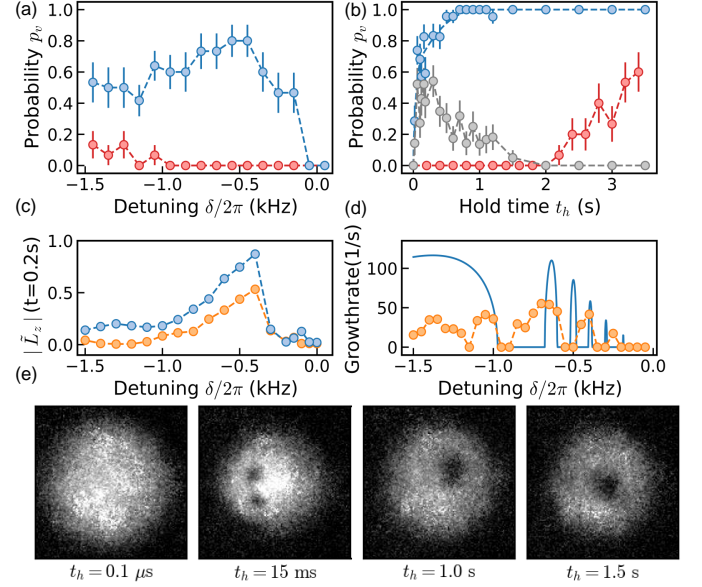


FIG. 2: (a) Probability of having vortices  $p_v$  vs. detuning  $\delta$  at  $t_h = 0.1 \mu\text{s}$  (red) and  $0.2$  s (blue). Finite  $p_v$  with  $t_h = 0.1 \mu\text{s}$  is attributed to the loading process. (b)  $p_v$  vs.  $t_h$  at  $\delta/2\pi = -600$  Hz (blue) and  $100$  Hz (red). Gray symbols show probability of having more than one vortices at  $\delta/2\pi = -600$  Hz. (c)  $|\tilde{L}_z|$  vs.  $\delta$  at  $t_h = 0.2$  s under a small cylindrical asymmetry calculated using 3D TDGPE with (blue) and without (orange) energy dissipation. Here  $\tilde{L}_z$  is the average of 10 simulations for each  $\delta$ . (d) Imaginary part of the Bogoliubov eigenspectrum for the excitation modes with OAM  $q = -2$  calculated for a 2D circularly symmetric system (blue) and the growth rate of the corresponding mode obtained by 3D TDGPE simulation (orange). (e) Atomic optical density (OD) vs.  $(x, y)$  for  $\delta/2\pi = -600$ Hz: except for  $t_h = 15$  ms, the deloading has  $\delta_{\text{del}}/2\pi = 2000$  Hz; at  $t_h = 15$  ms, the deloading has  $\delta_{\text{del}}/2\pi = 600$  Hz, see texts. The field of view is  $189 \times 189 \mu\text{m}^2$ .

the lowest-energy dressed state creates the gauge field  $\vec{A} = i\hbar\langle\xi_{-1}|\vec{\nabla}|\xi_{-1}\rangle$  effectively acting on atoms in this state (Fig. 1b). We obtain  $\vec{A} = A_{-1}(r)\hat{\phi}$  with  $rA_{-1} = \hbar[\delta/(\Omega(r)^2 + \delta^2)^{1/2} - 1]$  where we choose the gauge of  $|\xi_{-1}\rangle$  such that the BEC wave function is initially vortex-free. The ground-state's quasi-OAM is  $\ell_g = \pm\hbar$  and  $0$  for  $\pm\delta/2\pi > 200$  Hz and  $|\delta/2\pi| < 200$  Hz, respectively [33].

Our experiment starts with a BEC in  $|m_F = -1\rangle$  in a crossed dipole trap with  $N \approx 1.35 \times 10^5$  atoms. The trap frequencies along the  $x, y, z$  directions are  $(\omega_x, \omega_y, \omega_z)/2\pi = (120, 120, 157)$  Hz. The initial BEC in  $|m_F = -1\rangle$  has no vortex, which is adiabatically loaded into the lowest-energy Raman-dressed state with  $\ell = \hbar$  [33]: we turn on the Raman coupling in 7 ms followed by ramping the Raman detuning from  $\delta_i = \delta + 2\pi \times 2600$  Hz to  $\delta$  with the rate  $d\delta/dt = -2\pi \times 178.6$  Hz/ms. The value of  $\delta$  tunes the implemented  $A_{-1}(r)$ . We then hold the system at  $\delta$  for  $t_h$ , and probe the atoms by “deloading” [33, 37]. Such adiabatic de-

loading maps the lowest energy dressed state to the single spin  $|m_F = -1\rangle$ , which is ramping the detuning from  $\delta$  to  $\delta_{\text{del}} = \delta + 2\pi \times 2600$  Hz with the same  $|d\delta/dt|$  followed by turning off the Raman coupling in 7 ms. After a 23.9 ms time of flight we image the atoms. Although the local gauge transformation changes the gauge potential and the BEC wave function, deloading to  $|m_F = -1\rangle$  means using the gauge of  $|\xi_{-1}\rangle$  where the initial BEC wave function is vortex-free.

Since the initial state's  $\ell = \hbar$  differs from  $\ell_g(\delta)$  for  $\delta/2\pi < 200$  Hz, the condensate can temporally evolve if there are instabilities. They can be dynamical instabilities where states can evolve under zero temperature or no dissipation, or Landau instabilities under dissipation.

We first investigate the probability of having vortices,  $p_v$ , with various  $\delta$  and  $t_h$ . We repeat the experiment by 15 times at given  $(\delta, t_h)$ , identify for each image whether the BEC has vortices or not from the density dip signifying the phase singularity of a vortex, and derive the probability  $p_v$  [42]. Fig. 2a shows the  $\delta$  dependence of  $p_v$ . At  $t_h = 0.2$  s, vortices appear with high probability at  $\delta < 0$ , and  $p_v$  peaks at  $\delta/2\pi \sim -500$  Hz. To study the dynamics, we measure  $p_v$  vs.  $t_h$  at  $-600 \lesssim \delta/2\pi \lesssim 100$  Hz, where Fig. 2b shows data of  $\delta/2\pi = -600$  and 100 Hz. For  $\delta/2\pi = 100$  Hz, there is no vortex nucleation until  $t_h \gtrsim 2.0$  s, whereas  $p_v$  at  $\delta/2\pi = -600$  Hz starts increasing from  $t_h = 0$ . From  $p_v(t_h = 0.2$  s) we find the threshold detuning of vortex nucleation is  $\delta_{\text{thr}}/2\pi \sim -50(50)$  Hz. We note that  $\delta_{\text{thr}}/2\pi$  is significantly below 200 Hz, which is the critical detuning for thermodynamically stable  $\ell = 0$  state.

We also plot the probability of having more than one vortex,  $p_{v, N_v > 1}$ , vs.  $t_h$  for  $\delta/2\pi = -600$  Hz in Fig. 2b, which shows that the appearance of multiple vortices is a signature of the early stage of vortex nucleation. At sufficiently long  $t_h$ ,  $p_{v, N_v > 1} = 0$  indicates the system has single vortex in the deloaded  $|m_F = -1\rangle$ . For  $\delta/2\pi = 100$  Hz,  $p_{v, N_v > 1} = 0$  always holds, and the vortex nucleation at  $t_h \gtrsim 2.0$  s without dynamical instability may be explained by effects of thermal atoms [18].

The  $\delta$  dependence of  $p_v$  well reflects the initial change of the system's OAM. We numerically solve the 3D time-dependent Gross-Pitaevskii equation (TDGPE) and calculate the time evolution of the OAM  $\tilde{L}_z$  of the in-situ wave function projected onto the spinor state  $|\xi_{-1}\rangle$ . The TDGPE starts from the initial spin-polarized state with random noise. Fig. 2c shows  $|\tilde{L}_z|$  vs.  $\delta$  at  $t_h = 0.2$  s, which has a similar peak structure as Fig. 2a. Here, we incorporate the cylindrical asymmetry of the Raman coupling  $\Omega$  arising from that of the LG beam and add a phenomenological energy dissipation. We find the asymmetry allows for change of  $|\tilde{L}_z| \sim 0.5\hbar$ . The dissipation further enhances the change of  $|\tilde{L}_z|$ .

Our vortex nucleation is triggered by the dynamical instability of a localized mode at the trap center. As shown in Fig. 1b, the azimuthal velocity around the

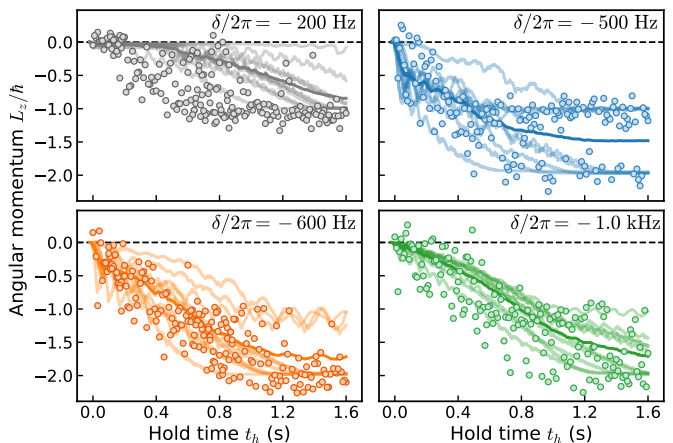


FIG. 3: Angular momentum vs.  $t_h$  of the atoms deloaded to  $m_F = -1$  at  $\delta/2\pi = -200, -500, -600, -1000$  Hz. Symbols denote the experimental data  $L_z$ ; light-colored curves denote ten individual simulations of  $\tilde{L}_z$  and the dark-colored ones indicate the average for each detuning.

trap center increases as  $\delta$  decreases. When it exceeds the critical velocity, the Landau instability arises, i.e., the Bogoliubov-de Gennes (BdG) mode localized at the trap center has a negative frequency (see supplement). With varying  $\delta$ , the localized mode couples with one of the other positive-frequency modes, leading to dynamical instability. Thus, our system is distinct from those under uniform synthetic magnetic fields with the velocity peaked at the condensate's periphery, where vortices are nucleated. Our present system has localized synthetic magnetic fields and the associated localized velocity field near the trap center, where vortex nucleation starts. Fig. 2d shows the imaginary part of the lowest-frequency BdG eigenmode with the OAM  $q = -2$  in 2D cylindrically symmetric systems. The nonzero imaginary part arises at  $\delta/2\pi \lesssim -200$  Hz. We also confirm the existence of the dynamical instability in 3D from the exponential growth of the annular  $q = -2$  Fourier component of the wave function from TDGPE for cylindrically symmetric 3D systems (see supplement). We note that the dynamical instability inherently exists even in cylindrically symmetric systems, in strong contrast to mechanically rotating BECs. Further, dissipation can induce nucleations via Landau instability: Simulations with asymmetry for  $|\tilde{L}_z|(t_h = 0.2$  s) in Fig. 2c shows  $|\tilde{L}_z|$  is larger in the presence of dissipation for  $\delta/2\pi \lesssim -350$  Hz.

To probe the initial change of the atomic state, we image the atoms with a small  $t_h \approx 15$  ms and  $\delta/2\pi = -600$  Hz. We choose a smaller final detuning  $\delta_{\text{del}}$  so that the configuration of the phase singular points changes less during the deloading process, and observe a pair of density dips come closer to the trap center. Together with the measured OAM  $\sim 0$  (see below), the experimental data indicates that a vortex-antivortex pair (see Fig. 2e) is generated at the trap center, agreeing with

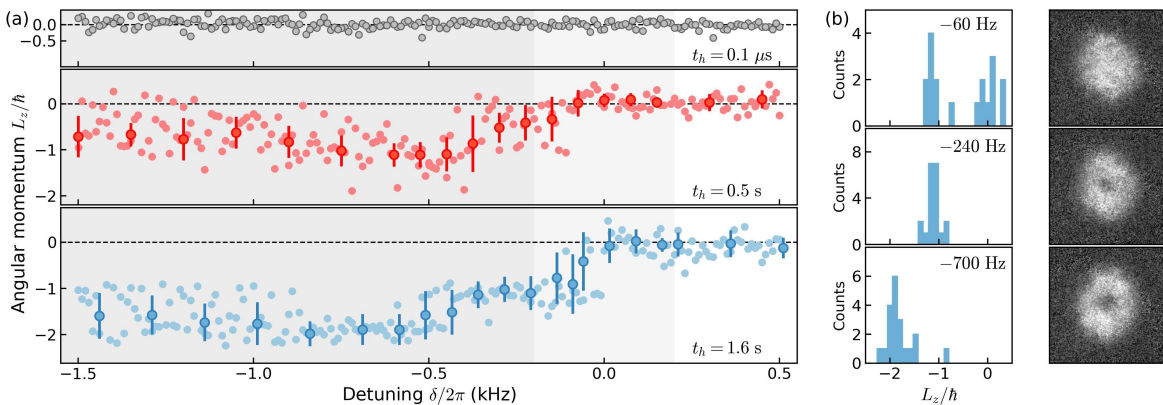


FIG. 4: (a) Angular momentum  $L_z$  of atoms deloaded to  $m_F = -1$  versus detuning at various hold time,  $t_h = 0.1 \mu\text{s}$ ,  $0.5 \text{ s}$  and  $1.6 \text{ s}$ . The data with a negligibly small  $t_h = 0.1 \mu\text{s}$  indicate that  $L_z$  remains about zero during the loading and deloading process. Average and standard deviation of 15 points taken at each  $\delta$  are also displayed for  $t_h = 0.5 \text{ s}$  and  $1.6 \text{ s}$ . The background colors indicate the ground state phases of  $\ell_g = \hbar$  (white),  $0$  (light gray) and  $-\hbar$  (gray). (b) Histograms of  $L_z$  (left) and the examples of ODs in the  $xy$  plane at  $\delta/2\pi = -60, -240, -700 \text{ Hz}$  and  $t_h = 1.6 \text{ s}$ . The ODs are for states with  $L_z \approx 0, -\hbar$ , and  $-2\hbar$ , respectively. The field of view is  $210 \times 210 \mu\text{m}^2$ .

the simulation. The appearance of the vortex-antivortex pair can be understood by noting that in the  $\delta \rightarrow -\infty$  limit a doubly quantized vortex is imprinted in the bare spin  $|m_F = 1\rangle$  component [38]. A doubly quantized vortex is dynamically unstable against splitting [39, 40], i.e., against the growth of  $q = -2$  mode. After the vortex splits, the deloading process additionally imprints a doubly quantized vortex with the opposite winding, which corresponds to the appearance of two vortex pairs in the  $|m_F = -1\rangle$ . Differing from Ref. [38], we investigate the instability occurring at  $\delta \lesssim 0$  with a small  $|\delta|$  and observe the dynamics for a longer duration. During the time evolution, the generated vortex and anti-vortex are pair-annihilated, recreated, or depart from each other depending on the values of  $\delta$  and  $t_h$ . At small  $t_h \approx 15 \text{ ms}$  we observe only one vortex pair, suggesting one of the vortex pairs is soon pair-annihilated. Subsequently, the asymmetry and dissipation allow the system to emit one vortex or two vortices, where  $L_z$  reaches  $-\hbar$  or  $-2\hbar$ , respectively. The system can thus reach the ground state.

Next, we measure the OAM of the atoms deloaded to  $|m_F = -1\rangle$ , which is  $L_z = \ell - \hbar$ , from the quadrupole mode precession rate [6, 41]. The quadrupole mode precession angle  $\theta$  after TOF is given by  $\theta = L_z/2m\langle R_\perp^2 \rangle(\tau + \tau_{\text{exp}})$ , where  $L_z/2m\langle R_\perp^2 \rangle$  is the in-trap precession rate [41],  $R_\perp$  is the transverse size,  $\tau_{\text{exp}}$  is an additional time accounting for the precession during TOF. We calibrate  $L_z$  from measured  $\theta$  for atoms with definite  $L_z = 0, -2\hbar$ , respectively, vs. hold time  $t_h$  (see supplement). Then we apply linear interpolation to derive  $L_z$  from  $\theta$  without using the theoretical formula. Fig. 3 illustrates the  $t_h$  dependence of  $L_z$  for  $\delta/2\pi = -200, -500, -600$ , and  $-1000 \text{ Hz}$ .  $L_z = \ell - \hbar$  can reach  $-2\hbar$  for  $\delta/2\pi = -500, -600, -1000 \text{ Hz}$ , which is consistent with  $L_z = \ell_g - \hbar$  and  $\ell_g = -\hbar$ . In Fig. 3,

we also show the numerical results of TDGPE with the asymmetry of  $\Omega$  and dissipation, where we determine the magnitude of the dissipation to agree with the experimental data at  $\delta/2\pi = -600 \text{ Hz}$ . The numerical data reasonably agrees with the experiment also for  $\delta/2\pi = -500$  and  $-1000 \text{ Hz}$ , but the dynamics proceeds slower for  $\delta/2\pi = -200 \text{ Hz}$ , suggesting a  $\delta$ -dependent dissipation.

We also measure the  $\delta$  dependence of  $L_z$  for  $t_h = 0.1\mu, 0.5, 1.6 \text{ s}$  (Fig. 4). From Fig. 4a, we find  $\delta_{\text{thr}} \lesssim 0$ , consistent with the  $p_v$  data in Fig. 2a. The data at  $t_h = 1.6 \text{ s}$  has plateaus at  $0, -\hbar, -2\hbar$  where the standard deviations of  $L_z$  are relatively small,  $\approx 0.2\hbar$ , and are close to the typical uncertainty of  $L_z$  for the case when BECs have stable  $L_z$ . For the detunings at transitions between the plateaus, the standard deviations of  $L_z$  are relatively large, correspondingly, the histogram of  $L_z$  has two peaks (see the top panel of Fig. 4b). This behavior is also shown in the  $\delta/2\pi = -500 \text{ Hz}$  data of Fig. 3.

In conclusion, we observe vortex nucleations in spinor BECs which are initiated by a spatially localized unstable mode, owing to an azimuthal velocity fields that peaks near the trap center. A vortex-antivortex pair creation near the center signifies the dynamically unstable mode that leads to vortex nucleations. The experimental data is consistent with numerical simulations which show both dynamical and Landau instabilities. We present the first experimental characterization of OAM's time evolution during vortex nucleations. We may extend the current work to more versatile vortex configurations with dynamical manipulations and higher order Raman vortex laser beams with  $\Delta\ell > 1$ . Our calculations show that one may produce instability at  $\delta > 0$  with sufficiently large  $\Delta\ell$ . The location of the peak of the velocity field at  $r = r_{\text{max}}$  can be engineered, and one expects unstable

surface modes for system size  $R < r_{\max}$  and localized modes for  $R > r_{\max}$ , and intriguing competitions between these two mechanisms.

The authors thank C. Chin, W. D. Phillips and I. B. Spielman for useful discussions. We also thank N. C. Chiu for critical readings of the manuscript, and thank H. C. Yao, T. H. Chien and Y. H. Su for their technical assistance. Y. -J. L. was supported by MOST 108-2112-M-001-033-MY3 and 111-2112-M-001-048-MY3 and the Thematic Research Program of Academia Sinica S. -K. Y. was supported by MOST 110-2112-M-001-051-MY3. Y. K. was supported by JSPS KAKENHI (Grant Nos. JP19H01824, and JP21H01009).

- 
- [1] J. Dalibard, F. Gerbier, G. Juzeliūnas, and P. Öhberg, *Rev. Mod. Phys.* **83**, 1523 (2011).
- [2] V. Galitski and I. B. Spielman, *Nature* **494**, 49 (2013).
- [3] N. Goldman, G. Juzeliūnas, P. Öhberg, and I. B. Spielman, *Rep. Prog. Phys.* **77**, 126401 (2014).
- [4] H. Zhai, *Reports on Progress in Physics* **78**, 026001 (2015).
- [5] K. W. Madison, F. Chevy, W. Wohlleben, and J. Dalibard, *Phys. Rev. Lett.* **84**, 806 (2000).
- [6] F. Chevy, K. W. Madison, and J. Dalibard, *Phys. Rev. Lett.* **85**, 2223 (2000).
- [7] J. R. Abo-Shaeer, C. Raman, J. M. Vogels, and W. Ketterle, *Science* **292**, 476 (2001).
- [8] V. Schweikhard, I. Coddington, P. Engels, V. P. Mogen-dorff, and E. A. Cornell, *Phys. Rev. Lett.* **92**, 040404 (2004).
- [9] N. Cooper, *Advances in Physics* **57**, 539 (2008).
- [10] D. Guéry-Odelin, *Phys. Rev. A* **62**, 033607 (2000).
- [11] P. C. Haljan, I. Coddington, P. Engels, and E. A. Cornell, *Physical Review Letters* **87**, 210403 (2001).
- [12] Y. J. Lin, R. L. Compton, K. Jimenez-Garcia, J. V. Porto, and I. B. Spielman, *Nature* **462**, 628 (2009).
- [13] A. J. Leggett, *Reviews of Modern Physics* **73**, 307 (2001).
- [14] K. W. Madison, F. Chevy, V. Bretin, and J. Dalibard, *Phys. Rev. Lett.* **86**, 4443 (2001).
- [15] F. Chevy, K. W. Madison, V. Bretin, and J. Dalibard, *SpringerLink* pp. 109–124 (2002).
- [16] E. Hodby, G. Hechenblaikner, S. A. Hopkins, O. M. Maragò, and C. J. Foot, *Physical Review Letters* **88**, 010405 (2001).
- [17] S. Sinha and Y. Castin, *Phys. Rev. Lett.* **87**, 190402 (2001).
- [18] C. Lobo, A. Sinatra, and Y. Castin, *Phys. Rev. Lett.* **92**, 020403 (2004).
- [19] F. Dalfovo and S. Stringari, *Phys. Rev. A* **63**, 011601 (2000).
- [20] T. P. Simula, S. M. M. Virtanen, and M. M. Salomaa, *Phys. Rev. A* **66**, 035601 (2002).
- [21] A. L. Fetter, *Reviews of Modern Physics* **81**, 647 (2009).
- [22] K. Kasamatsu, M. Tsubota, and M. Ueda, *Phys. Rev. A* **67**, 033610 (2003).
- [23] E. Lundh, C. J. Pethick, and H. Smith, *Physical Review A* **55**, 2126 (1997).
- [24] A. Ramanathan, K. C. Wright, S. R. Muniz, M. Zelan, W. T. Hill, C. J. Lobb, K. Helmerson, W. D. Phillips, and G. K. Campbell, *Physical Review Letters* **106**, 130401 (2011).
- [25] S. Moulder, S. Beattie, R. P. Smith, N. Tammuz, and Z. Hadzibabic, *Phys. Rev. A* **86**, 013629 (2012).
- [26] S. Beattie, S. Moulder, R. J. Fletcher, and Z. Hadzibabic, *Physical Review Letters* **110**, 025301 (2013).
- [27] Y. Cai, D. G. Allman, P. Sabharwal, and K. C. Wright, *Phys. Rev. Lett.* **128**, 150401 (2022).
- [28] G. Del Pace, K. Khani, A. Muzi Falconi, M. Fedrizzi, N. Grani, D. Hernandez Rajkov, M. Inguscio, F. Scazza, W. J. Kwon, and G. Roati, *Phys. Rev. X* **12**, 041037 (2022).
- [29] L. J. LeBlanc, K. Jiménez-García, R. A. Williams, M. C. Beeler, W. D. Phillips, and I. B. Spielman, *New Journal of Physics* **17**, 065016 (2015).
- [30] R. M. Price, D. Trypogeorgos, D. L. Campbell, A. Putra, A. Valdés-Curiel, and I. B. Spielman, *New Journal of Physics* **18**, 113009 (2016).
- [31] L. B. Taylor, R. M. W. van Bijnen, D. H. J. O’Dell, N. G. Parker, S. J. J. M. F. Kokkelmans, and A. M. Martin, *Phys. Rev. A* **84**, 021604 (2011).
- [32] H.-R. Chen, K.-Y. Lin, P.-K. Chen, N.-C. Chiu, J.-B. Wang, C.-A. Chen, P.-P. Huang, S.-K. Yip, Y. Kawaguchi, and Y.-J. Lin, *Physical Review Letters* **121**, 113204 (2018).
- [33] P.-K. Chen, L.-R. Liu, M.-J. Tsai, N.-C. Chiu, Y. Kawaguchi, S.-K. Yip, M.-S. Chang, and Y.-J. Lin, *Physical Review Letters* **121**, 250401 (2018).
- [34] D. Zhang, T. Gao, P. Zou, L. Kong, R. Li, X. Shen, X.-L. Chen, S.-G. Peng, M. Zhan, H. Pu, et al., *Physical Review Letters* **122**, 110402 (2019).
- [35] D. R. Murray, S. M. Barnett, P. Öhberg, and D. Gomila, *Phys. Rev. A* **76**, 053626 (2007).
- [36] D. R. Murray, P. Öhberg, D. Gomila, and S. M. Barnett, *Phys. Rev. A* **79**, 063618 (2009).
- [37] R. A. Williams, L. J. LeBlanc, K. Jiménez-García, M. C. Beeler, A. R. Perry, W. D. Phillips, and I. B. Spielman, *Science* **335**, 314 (2012).
- [38] Y. Shin, M. Saba, M. Vengalattore, T. A. Pasquini, C. Sanner, A. E. Leanhardt, M. Prentiss, D. E. Pritchard, and W. Ketterle, *Phys. Rev. Lett.* **93**, 160406 (2004).
- [39] H. Pu, C. K. Law, J. H. Eberly, and N. P. Bigelow, *Phys. Rev. A* **59**, 1533 (1999).
- [40] M. Möttönen, T. Mizushima, T. Isoshima, M. M. Salomaa, and K. Machida, *Phys. Rev. A* **68**, 023611 (2003).
- [41] F. Zambelli and S. Stringari, *Physical Review Letters* **81**, 1754 (1998).
- [42] The uncertainty of  $p_v$  in the  $n = 15$  shots in Fig. 2 is given by  $\sigma/\sqrt{n}$  in the binomial distribution, where  $\sigma$  is the standard deviation of the  $n$  shots.
-

## Supplemental Materials: Vortex nucleations in spinor Bose condensates under localized synthetic magnetic fields

### FORMALISM OF THE DRESSED STATES AND ASSOCIATED GAUGE POTENTIALS

The Hamiltonian in the bare spin basis,  $|m_F = 1, 0, -1\rangle$ , in the frame rotating at  $\Delta\omega_L$  under rotating wave approximation in the  $(r, \phi, z)$  coordinate is

$$\hat{H}_{\text{lab}} = \left[ \frac{-\hbar^2}{2m} \frac{\partial}{r\partial r} \left( r \frac{\partial}{\partial r} \right) - \frac{\hbar^2}{2m} \frac{\partial^2}{\partial z^2} + \frac{L_z^2}{2mr^2} \right] \otimes \hat{1} + \vec{\Omega}_{\text{eff}} \cdot \vec{F}, \quad (\text{S1})$$

where  $F_x, F_y, F_z$  are the spin 1 matrices and  $L_z = -i\hbar\partial_\phi$ . Here, the effective Zeeman field from the Raman beams is  $\vec{\Omega}_{\text{eff}} = \Omega(r) \cos\phi \mathbf{e}_x - \Omega(r) \sin\phi \mathbf{e}_y + \delta \mathbf{e}_z$  given by the spin-OAM coupling where the OAM transfer is  $\Delta\ell = \hbar$  between  $|m_F\rangle$  and  $|m_F + 1\rangle$ .

For sufficiently large  $\vec{\Omega}_{\text{eff}} \cdot \vec{F}$ , the motional kinetic energy  $-(\hbar^2/2m)\nabla^2$  of the atoms is negligible and the energy eigenstates of the overall Hamiltonian are well approximated by the eigenstates of  $\vec{\Omega}_{\text{eff}} \cdot \vec{F}$ ,  $|\xi_n\rangle$ . Under this approximation, the atom's spinor wave function follows the local dressed eigenstate  $|\xi_n\rangle$ , whose quantization axis is along  $\vec{\Omega}_{\text{eff}}$ . The state of the dressed atoms is  $\langle \vec{r} | \Psi \rangle = \varphi_n(\vec{r}) |\xi_n(\vec{r})\rangle$ , where  $\varphi_n$  is the external part and  $|\xi_n\rangle$  is the normalized spin part of the wave function.  $|\varphi_n| = \sqrt{n_c}$  where  $n_c$  is the condensate density. The effective Hamiltonian for the external wave function  $\varphi_n$  is [S1]

$$H_{\text{eff}}^{(n)} = \frac{-\hbar^2}{2m} \frac{\partial}{r\partial r} \left( r \frac{\partial}{\partial r} \right) - \frac{\hbar^2}{2m} \frac{\partial^2}{\partial z^2} + \frac{(L_z - rA_n)^2}{2mr^2} + V(r) + \varepsilon_n + W_n. \quad (\text{S2})$$

Here  $L_z$  is the angular momentum operator and  $\vec{A} = i\hbar\langle \xi_n | \vec{\nabla} | \xi_n \rangle = A_n \hat{\phi}$  where  $A_n(r) = (i\hbar/r)\langle \xi_n | \partial_\phi \xi_n \rangle$  is the azimuthal gauge potential.  $V(r)$  is the spin-independent trap,  $\varepsilon_n = n\sqrt{\Omega(r)^2 + \delta^2}$  is the eigenenergy of  $\vec{\Omega}_{\text{eff}} \cdot \vec{F}$ , and  $W_n \approx \hbar^2/2mr^2$  is the geometric scalar potential. We label the lowest, middle, and highest energy dressed states as  $|\xi_{-1}\rangle, |\xi_0\rangle, |\xi_1\rangle$ , respectively. A general  $|\xi_{-1}\rangle$  is given by Euler rotations [S2]

$$|\xi_{-1}\rangle = e^{i(\bar{\theta} + \bar{\gamma})} \left( e^{i\phi} \frac{1 - \cos\beta}{2}, -\frac{\sin\beta}{\sqrt{2}}, e^{-i\phi} \frac{1 + \cos\beta}{2} \right)^T, \quad (\text{S3})$$

where  $\beta(r) = \tan^{-1}[\Omega(r)/\delta]$  is the polar angle of  $\vec{\Omega}_{\text{eff}}$ , and  $\bar{\theta} + \bar{\gamma}$  is the phase for gauge transformation. By choosing  $\bar{\theta} + \bar{\gamma} = 0$ , it leads to

$$A_{-1}^0 = \frac{\hbar}{r} \cos\beta. \quad (\text{S4})$$

Let  $\ell$  denote the angular momentum of  $\varphi_{-1}$  in this gauge. Then,  $\ell, \ell \pm \hbar$  are the mechanical angular momenta of the bare spin  $|m_F = 0, \pm 1\rangle$  components of the state  $\varphi_{-1}|\xi_{-1}\rangle$ , respectively. By using alternative gauges with  $\bar{\theta} + \bar{\gamma} = \pm\phi$ , it gives

$$A_{-1}^\pm = \frac{\hbar}{r} (\cos\beta \mp 1), \ell^\pm = \ell \mp \hbar, \quad (\text{S5})$$

where  $\ell^\pm$  is the angular momentum of the external wave function  $\varphi_{-1}$  in these gauges. The kinetic angular momentum is gauge independent, i.e.,  $\ell - rA_{-1}^0 = \ell^+ - rA_{-1}^+ = \ell^- - rA_{-1}^-$ . In our paper we choose  $\bar{\theta} + \bar{\gamma} = \phi$  such that the initial external wave function has  $\tilde{\ell} \equiv \ell^+ = 0$ , i.e., vortex-free, where

$$|\xi_{-1}\rangle = \left( e^{i2\phi} \frac{1 - \cos\beta}{2}, -e^{i\phi} \frac{\sin\beta}{\sqrt{2}}, \frac{1 + \cos\beta}{2} \right)^T \text{ with } \bar{\theta} + \bar{\gamma} = \phi, \quad (\text{S6a})$$

$$\tilde{\ell} = \ell - \hbar, \quad (\text{S6b})$$

$$A_{-1} = \frac{\hbar}{r} (\cos\beta - 1) = \frac{\hbar}{r} \left[ \frac{\delta}{(\Omega(r)^2 + \delta^2)^{1/2}} - 1 \right], \quad (\text{S6c})$$

and the external wave function has the phase  $\vartheta = (\tilde{\ell}/\hbar)\phi$ , leading to the azimuthal kinetic velocity

$$\begin{aligned} \vec{v}_{-1} &= m^{-1} (\hbar \vec{\nabla} \vartheta - A_{-1} \hat{\phi}) = m^{-1} \left( \frac{\tilde{\ell}}{r} - A_{-1} \right) \hat{\phi}, \\ v_{-1} &= m^{-1} \left( \frac{\tilde{\ell}}{r} - A_{-1} \right). \end{aligned} \quad (\text{S7})$$

## EXPERIMENTAL PROCEDURES AND METHODS

In the beginning of the experiment we produce a  $^{87}\text{Rb}$  BEC with  $N \approx 1.35 \times 10^5$  atoms in a crossed dipole trap in  $|F, m_F\rangle = |1, -1\rangle$  [S3]. The trap frequencies along  $\mathbf{e}_x, \mathbf{e}_y, \mathbf{e}_z$  directions are  $(\omega_x, \omega_y, \omega_z)/2\pi = (120, 120, 157)$  Hz. The smallest trap ellipticity  $\epsilon = (\omega_x^2 - \omega_y^2)/(\omega_x^2 + \omega_y^2)$  that we can reach is typically  $< 0.006$ . Then we adiabatically load the  $|m_F = -1\rangle$  BEC in the lowest energy Raman-dressed state, where the fraction in the excited dressed states are negligible. One of the two Raman beams is Gaussian (G) and the other one is Laguerre-Gaussian (LG). The beams are at  $\lambda = 790$  nm where their scalar light shifts from the D1 and D2 lines cancel. The G Raman beam has a waist  $\approx 200 \mu\text{m}$ , and the LG Raman produced by a vortex phase plate has a phase winding number  $m_\ell = 1$  and radial index of 0. The G and LG beams have frequencies of  $\omega_L$  and  $\omega_L + \Delta\omega_L$  and are linearly polarized along  $\mathbf{e}_y$  and  $\mathbf{e}_x$ , respectively. We estimate that the uncertainty of the relative position of the LG beam center  $O'$  to the BEC center  $O$  is  $\lesssim 0.4 \mu\text{m}$ .

We measure the angular momentum  $L_z$  of the atoms deloaded to  $|m_F = -1\rangle$  as the following: right after the deloading, we excite the surface quadrupole mode by abruptly changing the trap frequencies along the  $x', y'$  direction to  $120\sqrt{0.6}, 120\sqrt{1.6}$  Hz, respectively, where  $(x', y')$  has a 45 degree angle relative to  $(x, y)$ . This suddenly deforms the atoms to  $\epsilon' = (1.6 - 0.6)/(1.6 + 0.6) \approx 0.4545$ . We hold it at  $\epsilon'$  for 0.4 ms, and then suddenly change the trap frequencies back to 120 Hz in both directions, after which the quadrupole mode precesses within a delay time  $\tau$  up to 9 ms; finally the atoms are released for a 23.9 ms TOF. The typical value of  $\tau$  is 8.2 ms. Regarding the effects of deloading process on  $L_z$ , we measured  $L_z$  with the shortest adiabatic deloading time and with the longer deloading time that is used in our typical procedure, respectively. We confirm that the difference in  $L_z$  measured in the two time sequences is smaller than the uncertainty of  $L_z$ , which is  $\approx 0.2\hbar$ .

We adopt the feed-forward method to stabilize the magnetic bias field using fluxgate field sensors. After the BEC preparation we wait for the external trigger from the 60 Hz line, after which we apply feed-forward current signals into bias coils to cancel the field noise from 60 Hz harmonics. We also compensate the drifts of the DC magnetic field from the ambient and bias coils by measuring the field at the end of each experimental cycle and applying the feed-forward signal in the next cycle. Our typical field uncertainty is  $\lesssim 70$  Hz = 0.1 mG.

We compute the vortex nucleation probability as  $p_v = n_v/15$  where  $n_v$  is the number of experimental realizations with one or more than one vortices within the total of 15 realizations (the number of having no vortex is  $15 - n_v$ ). We identify vortices from the density dips signifying the phase singularity of a vortex. The vortex counting algorithm is based on Ref. [S4, S5] and references therein. We use a microwave field to selectively pump the atoms from  $|F = 1, m_F\rangle$  to  $|F = 2\rangle$  and perform resonant absorption imaging of  $F = 2 \rightarrow F' = 3$  transition. All the images shown in the paper are single-shot.

## DERIVATION OF THE ANGULAR MOMENTUM $L_z$ FROM THE QUADRUPOLE MODE PRECESSION

As a calibration for  $L_z$ , we measure the quadrupole mode precession angle  $\theta$  of the atoms deloaded to  $|m_F = -1\rangle$  with stable  $L_z = 0, -2\hbar$ , respectively, for the hold time  $0.1 \mu\text{s} < t_h < 1.6$  s. This allows for converting the  $\theta$  of a vortex-nucleated state to the  $L_z$ . To prepare the  $|m_F = -1\rangle$  with  $L_z = 0, -2\hbar$ , respectively, we load the condensate into the dressed state with quasi-angular momentum  $\ell = \ell_g = \hbar$  and  $-\hbar$ , respectively, hold  $t_h$  and then deload the atoms to  $m_F = -1$  with  $L_z = \ell - \hbar = 0$  and  $-2\hbar$ , respectively. Since the initial  $\ell$  equals to the absolute ground state's  $\ell_g$ ,  $\ell$  is unchanged during  $t_h$ , i.e., stable and without vortex nucleations. Therefore, the final  $L_z$  remains  $0, -2\hbar$  for  $\ell_g = \hbar, -\hbar$ , respectively, for all  $t_h$ . The precession angle is

$$\theta = \frac{L_z}{2m\langle R_\perp^2 \rangle}(\tau + \tau_{\text{exp}}), \quad (\text{S8})$$

where  $\theta_{\text{trap}} = L_z/2m\langle R_\perp^2 \rangle\tau$  is the precession angle in the trap for precession time  $\tau$  given by a sum rule approach [S6].  $R_\perp$  is the transverse size,  $R_\perp^2 = \langle x^2 + y^2 \rangle$  and  $\tau_{\text{exp}}$  is an additional time accounting for the precession during TOF expansion. Here, the precession angle during the excitation of quadrupole mode is negligibly small. We perform 3D TDGPE simulations for the quadrupole mode precession with  $0 < \tau \leq 8.2$  ms and 23.9 ms TOF for  $N \approx 1.3 \times 10^5$  atoms and  $L_z = 0, \hbar, 2\hbar$ , respectively. We find that  $\theta_{\text{trap}} \propto \tau$ ,  $\theta_{\text{trap}} \approx 14^\circ$  for  $(L_z = \hbar, \tau = 8.2$  ms) and  $\tau_{\text{exp}}$  contributes  $\approx 5^\circ$  to the overall  $\theta \approx 19^\circ$ , and  $\theta$  doubles for  $L_z = 2\hbar$ . Here,  $\tau_{\text{exp}}$  has significant contribution in the overall precession angle  $\theta$ .

In our experimental data of calibration,  $\theta_c(L_z = 0, -2\hbar)$ , we find two deviations from the simulations. First,  $\theta(L_z = 0)$  is theoretically zero, while our measured  $\theta_c(L_z = 0)$  is nonzero and slightly depends on  $t_h$ . Second, the

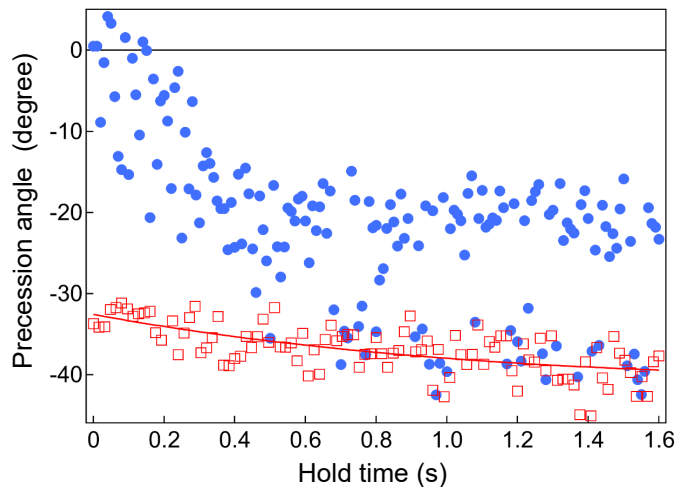


FIG. S1: Experimental data of the precession angles of the surface quadrupole mode vs. hold time  $t_h$ .  $\theta$  is for detuning  $\delta/2\pi = -500$  Hz (blue), which is the same as that in Fig. 3 of the paper. The magnitude of the angle for calibration  $\theta_c(-2\hbar) - \theta_c(0\hbar)$  (red) slightly increases with  $t_h$  due to the decrease of BEC number and the size  $R_\perp$ .

angle difference  $\theta_c(-2\hbar, t_h) - \theta_c(0\hbar, t_h)$  is about 85 % of that in the simulation. We identify that the deviation is largely from the precession angle during TOF, instead of that in the trap. We believe this is attributed to imperfect laser beam alignment. We assume the factor for the deviation of  $\theta_c(-2\hbar, t_h) - \theta_c(0\hbar, t_h)$  is independent of  $L_z$ , and derive  $L_z$  from  $\theta$  using linear conversions for all  $t_h$ ,

$$L_z = -2\hbar \frac{\theta - \theta_c(0\hbar)}{\theta_c(-2\hbar) - \theta_c(0\hbar)}, \quad (\text{S9})$$

see Fig. S1. The uncertainty of  $L_z$  for the measurements of  $L_z = 0, -2\hbar$  within 15 shots, where  $L_z$  is stable without vortex nucleations, is  $\approx 0.2\hbar$ .

### CYLINDRICAL ASYMMETRY OF THE RAMAN COUPLING

In the ideal condition for the Raman beams, both LG and G beam are cylindrically symmetric and the Raman coupling is denoted as

$$\vec{\Omega} = \Omega(r') \cos \phi' \mathbf{e}_x - \Omega(r') \sin \phi' \mathbf{e}_y + \delta \mathbf{e}_z, \quad (\text{S10})$$

$$\Omega(r') = \Omega'_M \sqrt{e} \frac{r'}{r_M} e^{-r'^2/2r_M^2}, \quad (\text{S11})$$

where the cylindrical coordinate  $(r', \phi')$  is with respect to the LG beam center  $O'$ ; the  $(\cos \phi', -\sin \phi')$  is for the order-one LG beam phase winding. Ideally,  $O'$  is identical to the BEC center  $O$ . While practically,  $O'$  can slightly deviate from  $O$  and that the intensity of LG beam is not perfectly cylindrical symmetric with respect to  $O'$ . Thus, the Raman coupling is

$$\vec{\Omega} = \Omega(r', \phi') \cos \phi' \mathbf{e}_x - \Omega(r', \phi') \sin \phi' \mathbf{e}_y + \delta \mathbf{e}_z, \quad (\text{S12})$$

$$\Omega(r', \phi') = \Omega'_M \sqrt{e} \frac{r'}{r_M} e^{-r'^2/2r_M^2} \left[ 1 + \sum_{\ell'=1}^{\ell'_{\max}} f(\ell') \cos(\ell' \phi' + \eta_{\ell'}) \right]. \quad (\text{S13})$$

The nonzero  $f(\ell')$  characterizes the LG beam intensity  $I_{LG}(\phi')$  and  $O'$  is displaced from  $O$  by up to  $0.4 \mu\text{m}$  with a random direction. We experimentally determined  $\Omega'_M, f(\ell'), \eta_{\ell'}$  by measuring  $\Omega(r', \phi')$  from BEC under Raman pulsing. We find that  $f(\ell' = 1) = 0.2$  and  $f(\ell') = 0.1/\ell'$  for  $2 \leq \ell' \leq \ell'_{\max} = 15$ ,  $(\eta_1 - \eta_2)/2\pi = 0.11 \pm 0.21$  and  $\eta_{\ell'}$  is random within  $[0, 2\pi]$  for  $3 \leq \ell' \leq \ell'_{\max} = 15$ .

## NUMERICAL SIMULATIONS

### Bogoliubov-de Gennes Spectrum in 2D

We solve the Bogoliubov-de Gennes (BdG) equation in the two-dimensional (2D) system. We first numerically obtain a stationary solution under the spin-OAM coupling with quasi OAM  $\ell = +\hbar$ , whose wave function is given by

$$|\Psi^{(0)}(r, \phi)\rangle \equiv \begin{pmatrix} \psi_1^{(0)}(r, \phi) \\ \psi_0^{(0)}(r, \phi) \\ \psi_{-1}^{(0)}(r, \phi) \end{pmatrix} = \begin{pmatrix} G_1(r)e^{i2\phi} \\ G_0(r)e^{i\phi} \\ G_{-1}(r) \end{pmatrix} = \underbrace{\begin{pmatrix} e^{i2\phi} & 0 & 0 \\ 0 & e^{i\phi} & 0 \\ 0 & 0 & 1 \end{pmatrix}}_{\equiv \mathcal{U}(\phi)} \begin{pmatrix} G_1(r) \\ G_0(r) \\ G_{-1}(r) \end{pmatrix}. \quad (\text{S14})$$

Here,  $G_{0,\pm 1}(r)$  are complex function of  $r$ , which are determined so that Eq. (S14) satisfies the stationary GPE. We choose the interaction parameters for the 2D system such that the Thomas-Fermi radius along the radial direction coincides with that in 3D.

We expand the order parameter around the obtained solution as

$$|\Psi(r, \phi, t)\rangle = e^{i\mu t/\hbar} \mathcal{U}(\phi) \left\{ \begin{pmatrix} G_1(r) \\ G_0(r) \\ G_{-1}(r) \end{pmatrix} + \sum_{q=0,\pm 1,\pm 2,\dots} \left[ e^{iq\phi - i\omega_q t} \underbrace{\begin{pmatrix} u_{1,q}(r) \\ u_{0,q}(r) \\ u_{-1,q}(r) \end{pmatrix}}_{\equiv |u_q(r)\rangle} + e^{-iq\phi + i\omega_q^* t} \underbrace{\begin{pmatrix} v_{1,q}^*(r) \\ v_{0,q}^*(r) \\ v_{-1,q}^*(r) \end{pmatrix}}_{\equiv |v_q^*(r)\rangle} \right] \right\} \quad (\text{S15})$$

By substituting Eq. (S15) into the TDGPE, and neglecting higher-order terms with respect to  $u_{m,q}(r)$  and  $v_{m,q}(r)$ , we obtain the BdG equation, which is written as in the following form:

$$\mathcal{H}_q \begin{pmatrix} |u_q(r)\rangle \\ |v_q(r)\rangle \end{pmatrix} = \hbar\omega_q \begin{pmatrix} |u_q(r)\rangle \\ |v_q(r)\rangle \end{pmatrix}, \quad (\text{S16})$$

$$\mathcal{H}_q \equiv \begin{pmatrix} \text{H}_q & \text{H}_{\text{od}} \\ -\text{H}_{\text{od}}^* & -\text{H}_{-q} \end{pmatrix}, \quad (\text{S17})$$

where  $\text{H}_q$  and  $\text{H}_{\text{od}}$  are  $3 \times 3$  Hermitian and symmetric matrices, respectively. Note that because we consider a circularly symmetric system, the BdG equation is block diagonal for each  $q$ . In addition, because of the particle-hole symmetry, i.e.,  $\mathcal{C}\mathcal{H}_q\mathcal{C}^{-1} = -\mathcal{H}_{-q}$  where  $\mathcal{C} = \tau_x K$  with  $\tau_x$  being the Pauli matrix in the Nambu space and  $K$  the complex conjugate operator, a state obtained by applying to  $\mathcal{C}$  to an eigenstate of  $\mathcal{H}_q$  with eigenvalue  $\hbar\omega_q$  is an eigenstate of  $\mathcal{H}_{-q}$  with eigenvalue  $-\hbar\omega_{-q}$ . It follows that the eigenmodes with  $q$  and  $-q$  are obtained from a single eigenvalue equation, and hence they are coupled.

We numerically solve the BdG equation for each  $q$  and obtain  $\omega_{q,n}$  where  $n$  is the energy level index. Figure S2 shows the BdG spectrum for  $-2 \leq q \leq 2$ . The lowest eigenfrequencies of  $q = -2$  and  $-1$ ,  $\omega_{-2,0}$  and  $\omega_{-1,0}$ , become negative in a certain range of  $\delta$ , and we plot  $-\omega_{-2,0}$  and  $-\omega_{-1,0}$  together with  $\omega_{2,n}$  and  $\omega_{1,n}$ , respectively. They have nonzero imaginary part when  $\text{Re}[\omega_{q,n} + \omega_{-q,0}] \sim 0$  [S7].

The imaginary part mainly comes from the coupling between the  $q = 2$  and  $-2$  modes. Here,  $\omega_{-2,0}$  becomes largely negative as  $\delta$  decreases. This is a localized mode at the center of the condensate: Since the atoms just after the loading process at largely negative  $\delta$  are almost in the  $|m_F = +1\rangle$  component, which has the phase winding  $e^{i2\phi}$  [see Eq. (S14)], the condensate density is strongly suppressed at  $r \sim 0$ ; The lowest-eigenfrequency mode of  $q = -2$  is the localized mode at the density dip. Hence, the instability associated with this mode affects mainly the center of the condensate. In Fig. S3, we show the wave function  $|\Psi^{(0)}(r, \phi)\rangle$  at  $\delta/2\pi = -450$  Hz (a) and

$$|\Psi(r, \phi)\rangle = |\psi^{(0)}(r, \phi)\rangle + 0.05\mathcal{U}(\phi) [e^{-i2\phi}|u_{-2,0}(r)\rangle + e^{i2\phi}|v_{-2,0}^*(r)\rangle], \quad (\text{S18})$$

at  $\delta/2\pi = -450$  (b) and  $-500$  Hz (c), for which  $\omega_{-2,0}$  has zero and nonzero imaginary part, respectively. Here, top and bottom panels show the density and phase profiles of the projected wave function onto  $|\xi_{-1}\rangle$ , which is defined by Eq. (S6a). One can see from Fig. S3(b) that the core mode with  $q = -2$  creates two density dips around the trap center, which correspond to two vortices with phase winding  $+1$ . In addition, due to our gauge choice, an additional phase winding of  $-2$  appears at the trap center, resulting in the appearance of two vortex-antivortex pairs after deloading. When  $\text{Im}\omega_{-2,0} \neq 0$  [Fig. S3(c)], the density at the medium radius is also modulated due to the coupling with the  $\omega_{2,n}$  mode. Although the unstable mode modulates the condensate density in the middle radius, it is hard to observe in experiments.

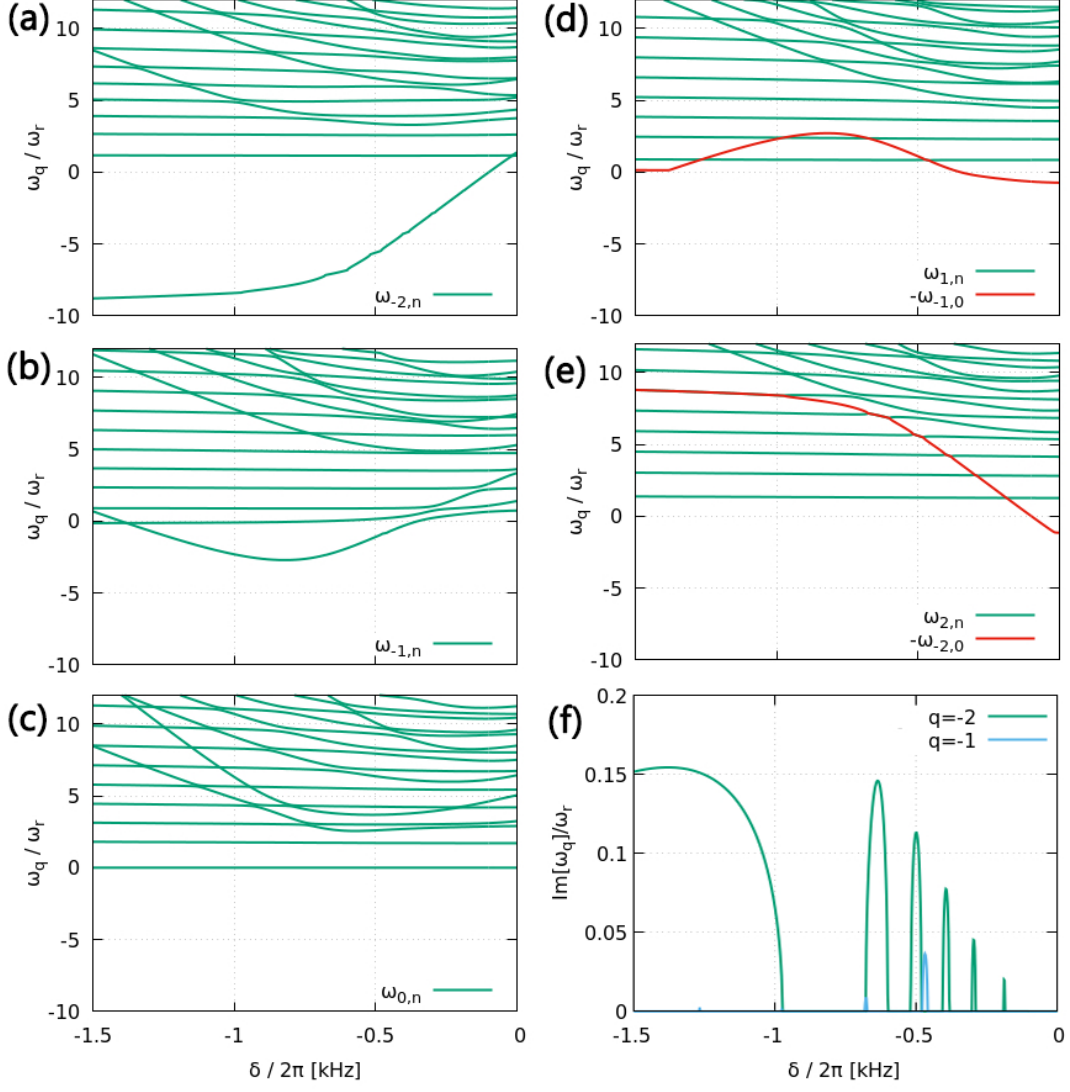


FIG. S2: (a)-(e) Real parts of the BdG spectrum for  $q = -2$  (a),  $-1$  (b),  $0$  (c),  $1$  (d), and  $2$  (e). (f) Imaginary parts of the eigenfrequency. In panels (d) and (e),  $-\omega_{-1,0}$  and  $-\omega_{-2,0}$  are also shown, respectively. Imaginary part arises when  $\text{Re}[\omega_{q,n} + \omega_{-q,0}] = 0$ .

### Dynamical instabilities in 3D

In order to confirm the appearance of dynamical instability in 3D, we numerically simulate the TDGPE and investigate the growth of fluctuations. We first calculate a stationary state under the SOAMC with a given  $\delta$  by fixing the quasi-OAM to be  $\ell = +\hbar$ , where the wave function for  $|m_F\rangle$  component is written as  $g_{m_F}(r, z)e^{i(m_F+1)\phi}$ . Here, we use the same harmonic potential as that in the experiment. We then prepare the initial order parameter by adding a  $q = -2$  component as

$$|\Psi^{(3D,ini)}(x, y, z)\rangle = \left[ \begin{pmatrix} g_1(r, z)e^{2i\phi} \\ g_0(r, z)e^{i\phi} \\ g_{-1}(r, z) \end{pmatrix} + \Delta_{\text{noise}} n(0, z)e^{-r^2/\xi^2} \begin{pmatrix} 1 \\ 0 \\ 0 \end{pmatrix} \right], \quad (\text{S19})$$

where  $n(0, z) = |g_{-1}(r = 0, z)|^2$  is the number density at  $r = 0$ , and we use  $\xi = 2.4 \mu\text{m}$  and  $\Delta_{\text{noise}} = 0.05$  ( $\Delta_{\text{noise}} = 0.2$ ) for  $\delta/2\pi > -0.8$  kHz ( $\delta/2\pi \leq -0.8$  kHz). Starting from the above initial state, we calculate the time evolution of the condensate  $|\Psi(x, y, z, t)\rangle$  with monitoring the angular Fourier component of the projected wave

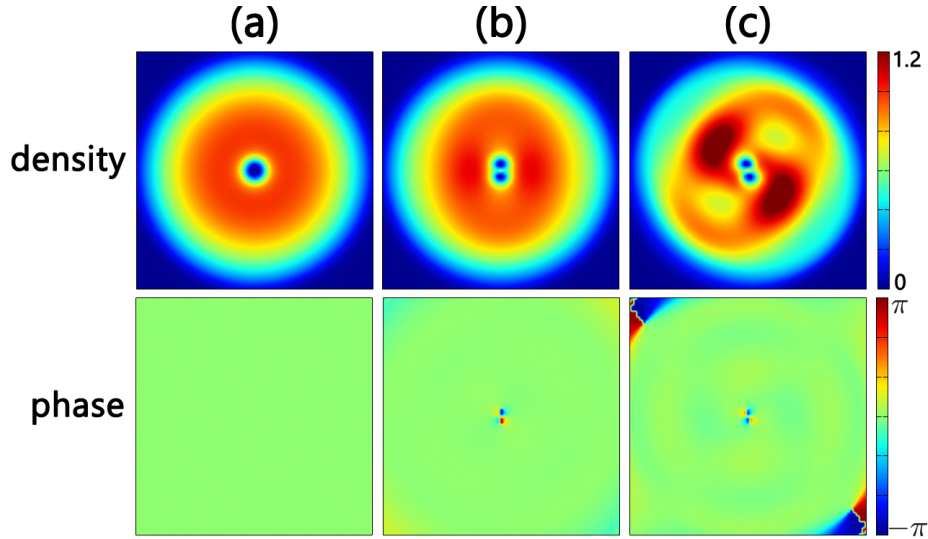


FIG. S3: Wave function of the stationary state with  $\ell = \hbar$ ,  $|\Psi^{(0)}(r, \phi)\rangle$ , at  $\delta/2\pi = -450$  Hz and those with the lowest-eigenfrequency BdG modes with  $q = -2$ , Eq. (S18), at  $\delta/2\pi = -450$  (b) and  $-500$  Hz (c), at which  $\omega_{-2,0}$  has zero and nonzero imaginary part, respectively. Shown are the density (top panels) and phase (bottom panels) profiles of the projected wave function onto the lowest-energy dressed state  $|\xi_{-1}\rangle$ . The density is normalized by the maximum of the total density without the BdG mode.

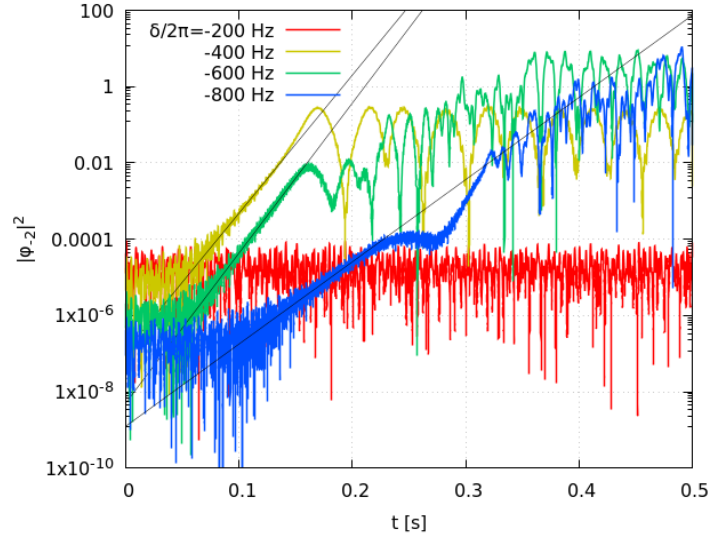


FIG. S4: Time evolution of the  $q = -2$  angular Fourier component of the wave function, Eq. (S20), starting from the initial wave function given in Eq. (S19). The thin black lines depict the fitting functions  $e^{a+bt}$  at  $\delta/2\pi = -400, -600,$  and  $-800$  Hz.

function onto  $|\xi_{-1}\rangle$ ,

$$\varphi_q = \int e^{-iq\phi} \langle \xi_{-1} | \Psi(x, y, z, t) \rangle dx dy dz. \quad (\text{S20})$$

Being consistent with the 2D BdG results,  $|\varphi_{-2}|^2$  exhibits exponential growth for certain values of  $\delta$ . Figure S4 shows the examples of the time evolution of  $|\varphi_{-2}|^2$ . We fit  $\log |\varphi_{-2}|^2$  for each  $\delta$  with a function  $f(t) = a + bt$  in a certain region of  $t$ . The 3D TDGPE data in Fig. 2d of the main text shows such obtained  $b$  for each  $\delta$ .

## Numerical simulations for long-time dynamics

Although dynamical instability triggers the instability, it cannot largely change the total orbital angular momentum as observed in the experiment. Within the BdG analysis, because the eigenmode with a complex eigenfrequency satisfies  $\int 2\pi r dr [\langle u_{q,n}(r)|u_{q,n}(r)\rangle - \langle v_{q,n}(r)|v_{q,n}(r)\rangle] = 0$ , the growth of the unstable mode does not lead to the change in  $L_z$ . In addition, a linearly unstable system does not always have nonlinear instability. In the present case, even when we see the appearance of two density dips in the projected wave function, they remain close at the center of the condensate.

After some calculations, we find that energy dissipation and cylindrical asymmetry are needed to reproduce the experimental results. The energy dissipation is phenomenologically introduced by replacing  $i\partial/\partial t$  in the TDGPE with  $(i - \gamma)\partial/\partial t$  with manually keeping the total number of atoms constant. For the simulations in Fig. 3 of the main text, we choose  $\gamma = 0.003$ . As for asymmetry, we incorporate two asymmetries that originally existed in the experiment: One is the shift of the LG beam from the trap center, and the other is the asymmetric power profile of the LG beam, which are included in the  $x, y$  dependence on the effective magnetic field as

$$\vec{\Omega}_{\text{eff}}(x, y) = \Omega(r', \phi')(\cos \phi', -\sin \phi', -\delta), \quad (\text{S21})$$

$$r' = \sqrt{[x - X(t)]^2 + y^2}, \quad (\text{S22})$$

$$\phi' = \arg[x - X(t) + iy], \quad (\text{S23})$$

where  $\Omega(r', \phi')$  is given in Eq. (S13). Here, without loss of generality, we choose the direction of the LG beam shift along the  $x$  axis and describe the amount of shift as  $X(t) = X_0 \cos(2\pi\nu_0 t + \eta_0)$  with  $X_0 = 0.4 \mu\text{m}$ ,  $\nu = 0.1 \text{ Hz}$ , and  $\eta_0$  being a uniform random number between 0 and  $2\pi$ .

### Initial deformation at the onset of vortex nucleations

We discuss the initial deformation of the condensate by investigating the detailed dynamics for the case of  $\delta/2\pi = -600 \text{ Hz}$ . Figure S5 shows the snapshots of the *in-situ* order parameter during the initial time evolution obtained by the 3D TDGPE simulations with asymmetry and energy dissipation. Here, each panel shows the density and phase profiles of the bare spin  $m_F = -1, 0$  and 1 components of the order parameter and those of the projected order parameter onto  $|\xi_{-1}\rangle$  in the  $z = 0$  plane. Just after loading the atoms to the lowest energy dressed state, a vortex with winding number 2 appears in the  $m_F = 1$  component ( $t_h = 0 \text{ ms}$ ), which soon splits into two single vortices ( $t_h = 15 \text{ ms}$ ) and rotates around the trap center ( $t_h = 30$  and  $45 \text{ ms}$ ). When we project the order parameter onto  $|\xi_{-1}\rangle$  (the right two columns), the density profile is similar to that of the  $m_F = 1$  component, but the projected order parameter has an additional unphysical phase winding  $-2$  around the LG beam center due to the gauge choice of  $|\xi_{-1}\rangle$ .

When we deload the dressed state to a positive  $\tilde{\delta}_{\text{del}}$ , the additional phase winding becomes physical, i.e., a vortex with winding number  $-2$  is imprinted in the  $m_F = -1$  component. In Fig. S6, we show the order-parameter change during the deloading process starting from  $t_h = 15 \text{ ms}$  in Fig. S5. Figure S6(a) is the results for deloading dynamics, where the detuning changes from  $\delta/2\pi = -600 \text{ Hz}$  to  $\tilde{\delta}_{\text{del}}/2\pi = 2 \text{ kHz}$  in  $14.56 \text{ ms}$ , followed by adiabatic turning off of Raman beams in  $7 \text{ ms}$ .  $t_{\text{del}}$  in Fig. S6 is the time from when we start the deloading, and the deloading process ends at  $t_{\text{del}} = 14.56 + 7 = 21.56 \text{ ms}$ . During the deloading process, a density dip appears in the projected order parameter at the phase winding point with winding  $-2$  ( $t_{\text{del}} = 4 \text{ ms}$ ), which is then combined with one of the single vortices with winding 1, becoming a vortex with winding  $-1$  ( $t_{\text{del}} = 6 \text{ ms}$ ). As a whole, a vortex-antivortex pair remains. During the residual time, the vortex configuration further changes and the distance between the vortex and antivortex becomes larger. When we deload to  $\tilde{\delta}_{\text{del}}/2\pi = 600 \text{ Hz}$  and shorten the total period for the deloading process to  $13.72 \text{ ms}$ , the vortices in the final state come closer to each other and are located closer to the trap center [Fig. S6 (b)].

Figure S7 shows the experimental results of  $\tilde{\delta}_{\text{del}}/2\pi = 2 \text{ kHz}$  (a) and  $600 \text{ Hz}$  (b) corresponding to  $m_F = -1$  component in the last row of Fig. S6 (a) and that in Fig. S6 (b), respectively. Being agreement with Fig. S6, the pair of density dips in Fig. S7 comes closer to the trap center and their distance becomes smaller for  $\tilde{\delta}_{\text{del}}/2\pi = 600 \text{ Hz}$  than in the case of  $\tilde{\delta}_{\text{del}}/2\pi = 2 \text{ kHz}$ . The experimentally measured  $L_z \approx 0$  (Fig. 3 of the main text) indicates the two vortices are a vortex and an antivortex, also in agreement with the simulation. Though Fig. S6 (simulation) and Fig. S7 (experiment) are before and after time-of-flight, respectively, we have numerically confirmed that the vortex configuration is almost unchanged during the time-of-flight.

At a longer  $t_h$ , we observe both experimentally and theoretically the cases when more than two vortices remain after deloading. Figure S8 shows an example of having four vortices, which is obtained by deloading to  $\tilde{\delta}_{\text{del}}/2\pi = 2 \text{ kHz}$

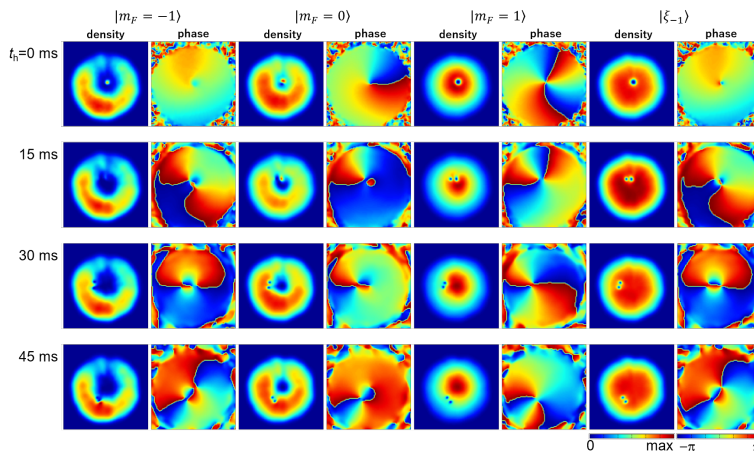


FIG. S5: *in-situ* time evolution during the holding time at  $\delta/2\pi = -600$  Hz numerically calculated with 3D TDGPE including asymmetry and energy dissipation. Shown are density  $|\psi_\alpha(x, y, 0, t)|^2$  and phase  $\arg[\psi_\alpha(x, y, 0, t)]$  profiles in the  $z = 0$  plane, where  $\psi_\alpha(x, y, z, t) \equiv \langle \alpha | \Psi(x, y, z, t) \rangle$  is the projection of the 3-component spinor order parameter  $|\Psi(x, y, z, t)\rangle$  onto the bare spin  $m_F$  state ( $|\alpha\rangle = |m_F = -1, 0, 1\rangle$ ) and the lowest-energy dressed state ( $|\alpha\rangle = |\xi_{-1}\rangle$ ). The color scale for the density profile is given by the maximum value in each panel. The panel size is  $17.4 \mu\text{m} \times 17.4 \mu\text{m}$ .

starting from  $t_h = 45$  ms in Fig. S5. In the long-time dynamics, the system reduces  $L_z$  by emitting some of the generated vortices and reaches the ground state with the aid of energy dissipation.

We note that in the above-explained dynamics, asymmetry as well as energy dissipation of the system are crucial. When the system is circularly symmetric, the vortex configuration is symmetric with respect to  $r = 0$ . In this case, it takes longer time for the splitting of a doubly quantized vortex in the  $m_F = 1$  component. Figure S9 shows the vortex dynamics during the deloading process starting from  $t_h = 500$  ms in the absence of asymmetry and energy dissipation. In the panels of  $t_{\text{del}} = 0$  ms, one can see that the initial deformation agrees well with that predicted by 2D BdG analysis [Fig. S3], and the vortex configuration is highly symmetric compared with, say,  $t_h = 45$  ms configuration in Fig. S5, even though we hold the condensate in the dressed state much longer time. During the deloading process, the two density holes in the projected order parameter soon disappear by combining with the imprinted vortex with winding  $-2$  at the LG beam center. Eventually, no vortex appears after deloading even at  $t_h = 500$  ms.

### AZIMUTHAL VELOCITY PROFILE

We show the azimuthal velocity for an atomic state whose spinor wave function is  $|\xi_{-1}\rangle$  or the  $\ell$ -dependent  $|\xi_g\rangle$  of the Gross-Pitaevskii (GP) ground state, respectively. Here we approximate our system as cylindrically symmetric.

The initial state has  $\ell = \hbar$ , i.e.,  $\tilde{\ell} = 0$  and vortex-free. This state is adiabatically prepared in the lowest-energy dressed state and is almost identical to the GP ground state. The detuning is  $-1500 < \delta/2\pi < 75$  Hz. We compute the spinor wave function  $|\xi_g(\ell)\rangle$  for  $\ell = \pm\hbar, 0$ , and compare them to  $|\xi_{-1}\rangle$ . For a not too small  $\delta > 0$ ,  $|\xi_{-1}\rangle$  is close to  $|\xi_g\rangle$  for  $\ell = \hbar$  provided  $|\langle \xi_{-1} | \xi_g \rangle|^2 \approx 1$ ; see Fig. S10. For  $\ell = 0, -\hbar$ ,  $|\langle \xi_{-1} | \xi_g \rangle|^2$  is small at small  $r$ , showing the deviation of  $|\xi_g, \ell = 0, -\hbar\rangle$  from  $|\xi_{-1}\rangle$ . As for  $\delta < 0$ ,  $|\xi_{-1}\rangle$  is close to  $|\xi_g\rangle$  for  $\ell = -\hbar$ . Due to a symmetry in the Hamiltonian,  $|\langle \xi_{-1} | \xi_g(\ell, \delta) \rangle| = |\langle \xi_{-1} | \xi_g(-\ell, -\delta) \rangle|$ .

For a general state  $|\psi\rangle = e^{i\tilde{\ell}\phi}|\xi\rangle$  in the gauge of Eq. (S6b), the azimuthal velocity is

$$v(r) = \langle \psi | \frac{\hbar}{imr} \partial_\phi \otimes \mathbf{1} | \psi \rangle, \quad (\text{S24})$$

which gives the same result of  $v_{-1}$  in Eq. (S7) for  $|\xi\rangle = |\xi_{-1}\rangle$ . The initial  $\ell = \hbar$  state has  $\tilde{\ell} = 0$  and thus  $v_{-1}(r) = -A_{-1}/m$ . As  $\delta$  decreases,  $A_{-1} < 0$  decreases monotonically and  $v_{-1}(r) > 0$  increases for any given  $r$ . This is just like the case of mechanically rotating BECs (before vortex nucleations) whose  $\ell \sim 0$  (nonzero due to small asymmetry of the stirring potential) with  $A = -m\Omega_{\text{stir}}r$  and the velocity is  $-A/m = \Omega_{\text{stir}}r$  that increases with  $\Omega_{\text{stir}}$ .

We then use Eq. (S24) to compute the velocity of the GP ground state  $v_g(r)$  for  $\ell = \pm\hbar, 0$ , respectively, and compare to  $v_{-1}(r)$ . For  $\delta > 0$ ,  $-\hbar \leq rA_{-1} \leq 0$ . Therefore,  $v_{-1}(\ell = \hbar) = -A_{-1}/m > 0$ ,  $v_{-1}(\ell = 0) = -\hbar/mr - A_{-1}/m < 0$

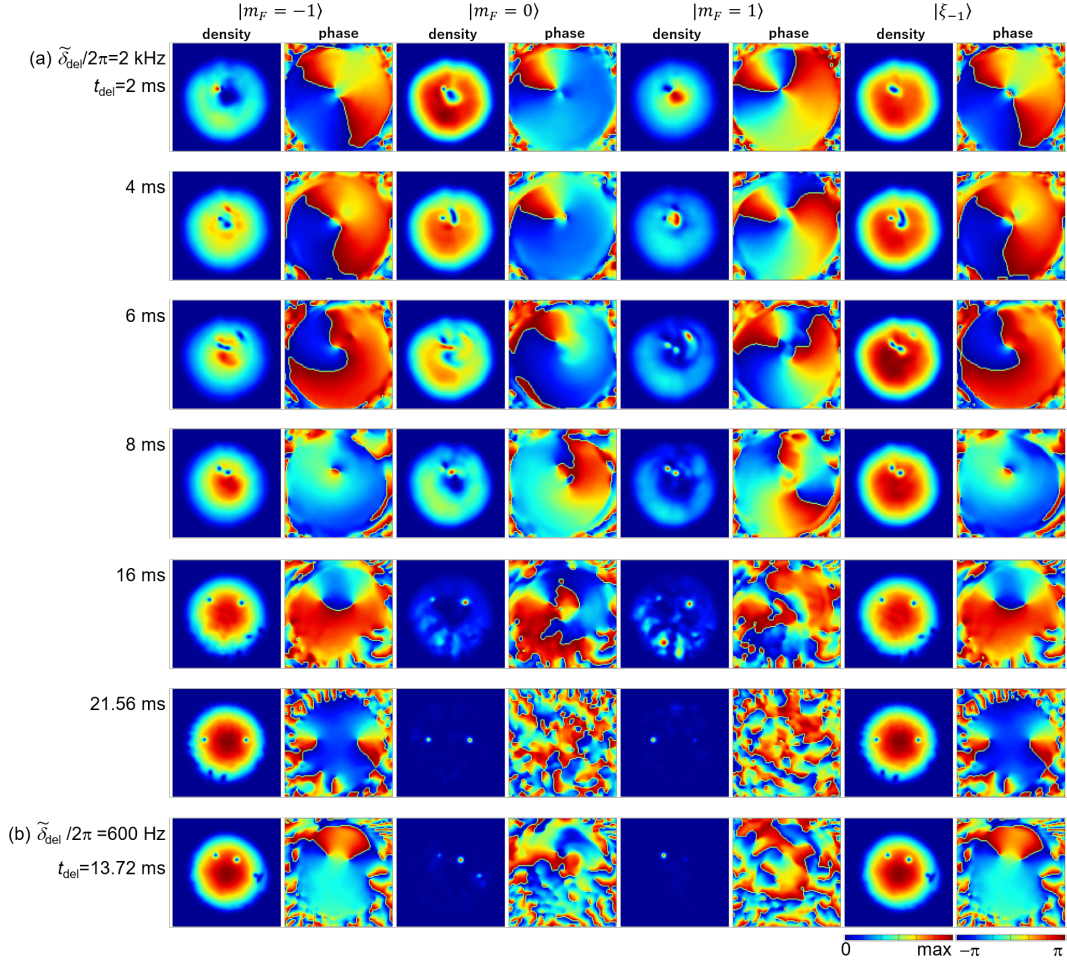


FIG. S6: *in-situ* time evolution during deloading starting from  $t_h = 15$  ms in Fig. S5 calculated in 3D TDGPE simulation with asymmetry and energy dissipation. The meaning of each panel is the same as that in Fig. S5. During deloading, we sweep the detuning  $\delta/2\pi = -600$  Hz to  $\tilde{\delta}_{\text{del}}/2\pi = 2$  kHz in 14.56 ms (a) and to  $\tilde{\delta}_{\text{del}}/2\pi = 600$  Hz in 6.72 ms (b) and then turn off the Raman beams in 7 ms.  $t_{\text{del}}$  is the time from when we start sweeping the detuning.

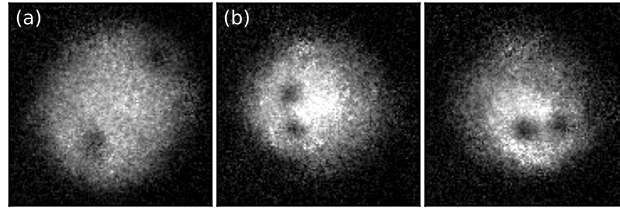


FIG. S7: Time-of-flight images of the initial dressed state with  $t_h \approx 15$  ms and  $\delta/2\pi = -600$  Hz after deloading to  $|m_F = -1\rangle$  with  $\tilde{\delta}_{\text{del}}/2\pi = 2$  kHz (a) and 600 Hz (b). The field of view is  $120 \mu\text{m} \times 120 \mu\text{m}$ .

and  $v_{-1}(\ell = -\hbar) = -2\hbar/mr - A_{-1}/m < 0$ . Similarly,  $v_g(\ell = \hbar) > 0$  and  $v_g(\ell = 0, -\hbar) < 0$ . We compare  $v_{-1}(r)$  and  $v_g(r)$  at  $\delta/2\pi = 250$  Hz in Fig. S11a, where it shows the absolute values of the velocities in the log scale. The unit of the dimensionless velocity is  $\omega_r a_{\text{HO}} = \sqrt{\hbar\omega_r/m} = 0.00074$  m/s with  $a_{\text{HO}} = \sqrt{\hbar/m\omega_r}$ . For  $\delta > 0$ ,  $v_{-1}(r)$  largely agrees with  $v_g(r)$  for  $\ell = \hbar$  even at small  $r$ . However, for  $\ell = 0, -\hbar$ ,  $v_{-1}(r) \propto 1/r$  near  $r = 0$ , which deviates from  $v_g(r)$ , and this is consistent with the results in Fig. S10. As  $r$  decreases,  $v_g(r, \ell = 0, -\hbar)$  stops increasing and decreases instead, showing a peak value at small  $r = r_{\text{max}} \sim 0.7 \mu\text{m}$ . This results from the fact that  $v_g(r = 0) = 0$  for the  $\ell = \pm\hbar, 0$  dressed states, which are coreless vortex states, i.e., one of the bare spin  $m_F$  component has zero

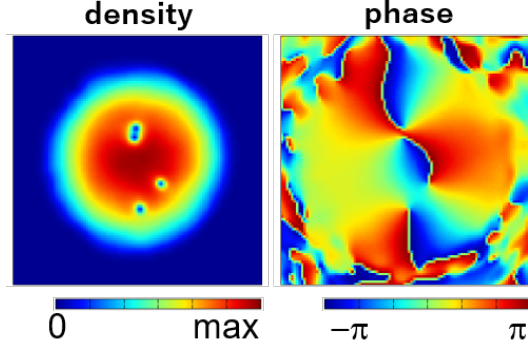


FIG. S8: *in-situ* order parameter in  $|m_F = -1\rangle$  in the  $z = 0$  plane after deloading to  $\tilde{\delta}_{\text{del}}/2\pi = 2$  kHz starting from  $t_h = 45$  ms in Fig. S5. In the numerical simulation, the asymmetry and energy dissipation of the system are included. Four vortices remain in the condensate, where two of them have phase winding  $+1$  and the other two have  $-1$ .

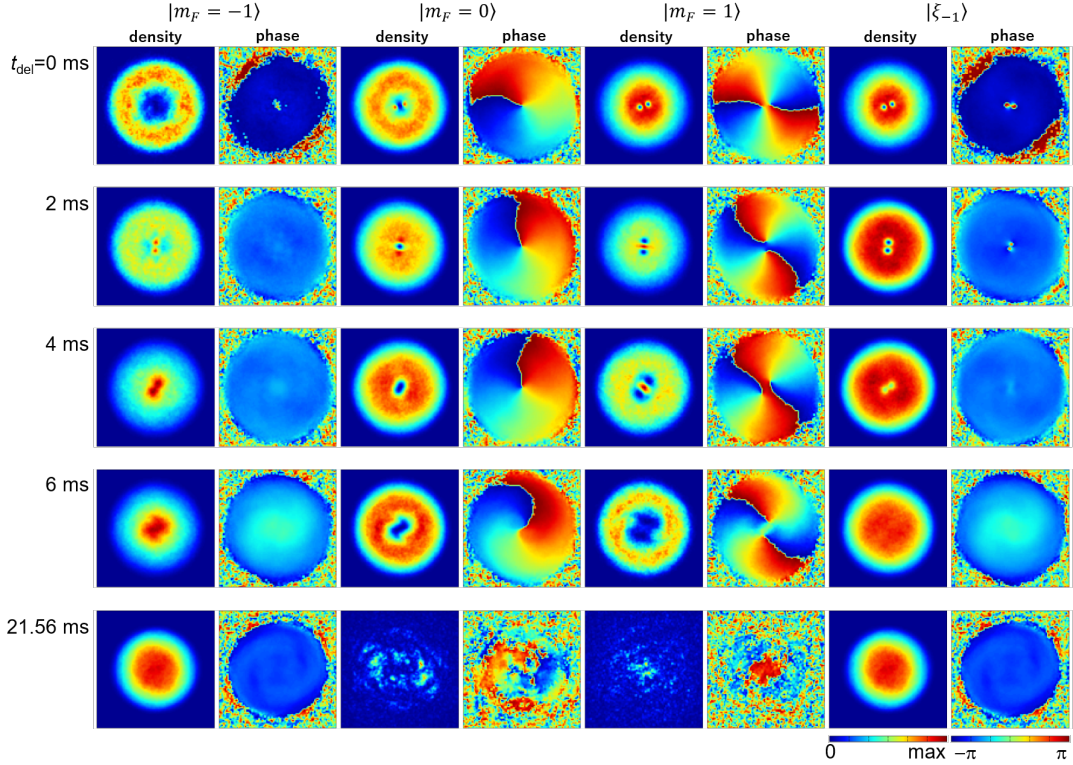


FIG. S9: Snapshots of 3D TDGPE simulation without asymmetry and energy dissipation. The meaning of each panel is the same as that in Fig. S5. The top panels are the state obtained by holding the condensate for  $t_h = 500$  ms at  $\delta/2\pi = -600$  Hz, and below are the time evolution during the deloading to  $\tilde{\delta}_{\text{del}}/2\pi = 2$  kHz.

OAM and contributes to nonzero density at  $r = 0$  with non-singular velocity  $v = 0$ .

Next we consider the detuning  $\delta < 0$ . We plot  $v_g(r, \ell = \hbar)$  of our initial state prior to vortex nucleations for  $\delta/2\pi = 250, 1, -250, -500$  Hz in Fig. S11b. For all  $\delta$ ,  $v_g(r)$  has a peak at small  $r_{\text{max}}$  which decreases with  $\delta$ . According to the 3D TDGPE simulations, the dynamical instability appears when  $\delta/2\pi \lesssim -200$  Hz, which indicates that negative energy excitations occur and the Landau criterion happens at  $\delta/2\pi \gtrsim -200$  Hz. In Fig. S11b the peak velocity of  $\delta/2\pi = -250$  Hz is  $\sim 1.5\omega_r a_{\text{HO}} \sim 0.0011$  m/s. We estimate the local sound velocity near the cloud center is about 0.0027 m/s for our peak mean field energy  $\sim 1.6$  kHz. We may argue that instability occurs when the peak of  $v_g(r, \ell = \hbar)$  equals to some numerical factor times the local sound speed.

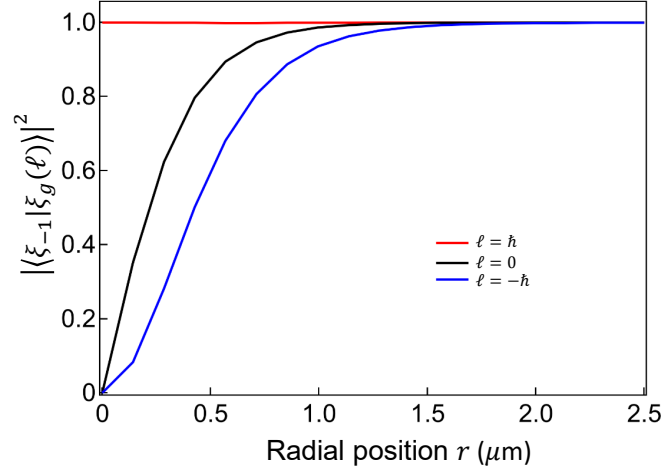


FIG. S10: The square of the inner product  $|\langle \xi_{-1} | \xi_g(\ell = 0, \pm \hbar) \rangle|^2$  for  $\delta/2\pi = 250$  Hz. Red, black and blue curves denote  $\ell = \hbar, 0, -\hbar$  for  $|\xi_g\rangle$ , respectively.

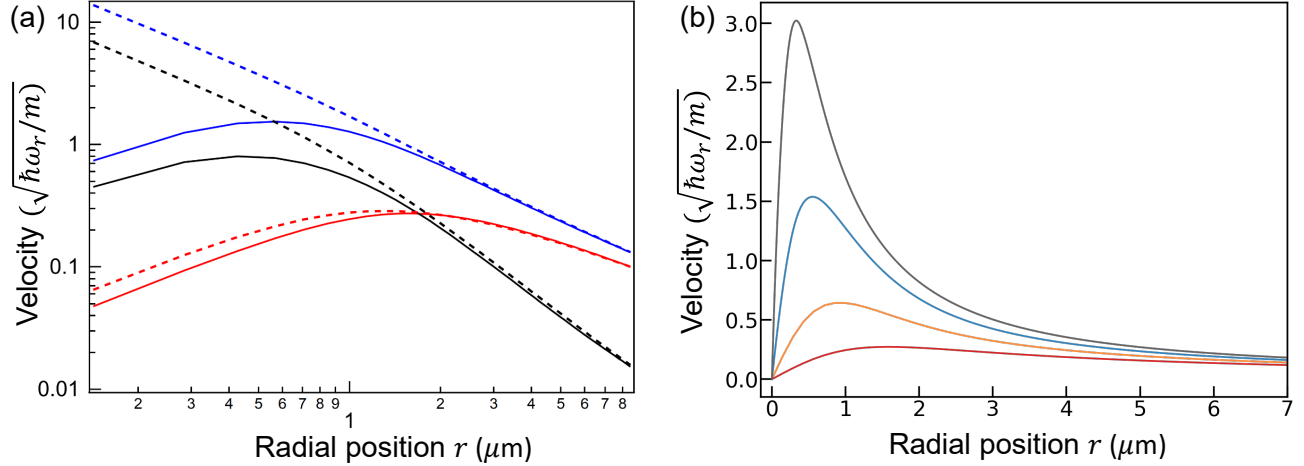


FIG. S11: (a) Absolute values of the azimuthal velocity  $v_{-1}(r)$  for  $|\xi_{-1}\rangle$  (dashed) and  $v_g(r)$  for  $|\xi_g\rangle$  (solid) at  $\delta/2\pi = 250$  Hz for  $\ell = \hbar, 0, -\hbar$ . The log scale plot shows  $v_{-1}, v_g$  for  $\ell = \hbar$  and  $-v_{-1}, -v_g$  for  $\ell = 0$  and  $-\hbar$ . Red, black and blue curves denote  $\ell = \hbar, 0, -\hbar$ , respectively. (b) Azimuthal velocity  $v_g(r)$  of the Gross-Pitaevskii ground state with  $\ell = \hbar$  for detuning  $\delta/2\pi = 250$  Hz (red), 1 Hz (orange),  $-250$  Hz (blue),  $-500$  Hz (grey).

Here we discuss the calculations showing the existence of instability at detuning  $\delta > 0$ , where one uses a high order LG beam to produce a Raman coupling with large  $\Delta\ell/\hbar$ . We choose the gauge of  $\bar{\theta} + \bar{\gamma} = (\Delta\ell/\hbar)\phi$  such that the initial state prior to vortex nucleations is vortex-free with  $\tilde{\ell} = \ell - \Delta\ell = 0$  and the velocity  $v_{-1}(r) = -A_{-1}(r)/m > 0$  increases with decreasing  $\delta$ . Fig. S12 shows  $-rA_{-1} = \Delta\ell[1 - \delta/(\Omega(r, \Delta\ell)^2 + \delta^2)^{1/2}]$  and the velocity  $v_{-1}$  vs.  $r$  for various  $\Delta\ell$  at  $\delta/2\pi = 200$  Hz. Here  $\Omega(r, \Delta\ell) = \Omega_M e^{\Delta\ell/2}(r/r_M)^{\Delta\ell} e^{-\Delta\ell r^2/2r_M^2}$  is the Raman coupling strength for a general  $\Delta\ell$ .  $v_{-1}$  has a peak value at the radial position  $r_{\max}$  that is determined by  $\delta$  and  $\Delta\ell$ . For  $\Delta\ell = 20\hbar$ , the peak of  $v_{-1}$  is  $\sim 0.0009$  m/s and is comparable to that in our experiment when negative energy excitations occur. One can tune  $r_{\max}$  to be small or large compared to the system size, which has unstable localized mode and surface mode, respectively. We then expect interesting competitions between the two physical mechanisms when  $r_{\max}$  is comparable to the system size.

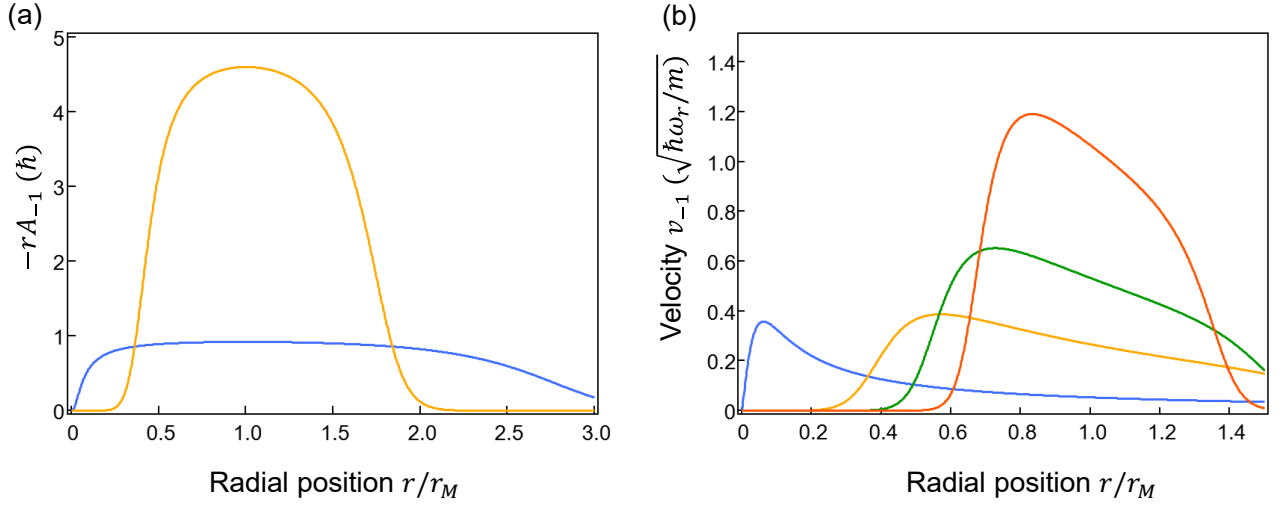


FIG. S12: Simulations for the lowest energy dressed state  $|\xi_{-1}\rangle$  with  $\delta/2\pi = 200$  Hz and the peak Raman coupling  $\Omega_M/2\pi = 2500$  Hz at  $r = r_M$  for various  $\Delta\ell$ . (a)  $-rA_{-1}$  vs.  $r/r_M$  for  $\Delta\ell = \hbar$  (blue) and  $5\hbar$  (orange) under the gauge where the BEC is initially vortex-free. (b) Azimuthal velocity  $v_{-1}$  vs.  $r/r_M$  for  $\Delta\ell = \hbar$  (blue),  $5\hbar$  (orange),  $10\hbar$  (green), and  $20\hbar$  (red).

### CHARACTERIZATION OF THERMAL ATOMS

We observe thermal atom numbers increase as the dressed state hold time  $t_h$  increases [S3]. The spinor wave function of the dressed state is labeled as  $|\xi_n\rangle$  where  $n = -1, 0, 1$  represents the lowest, middle and highest energy branches, respectively.  $N_n$  is the atom number in  $|\xi_n\rangle$ , including both the thermal and BEC components. The atoms in the excited dressed states  $|\xi_{0,1}\rangle$  are purely thermal without BEC component and their number fractions  $N_{0,1}/(N_{-1} + N_0 + N_1)$  increase with  $t_h$ . As for atoms in the lowest-energy branch  $|\xi_{-1}\rangle$ , it is a nearly pure condensate at  $t_h = 0$ , and the thermal number fraction within  $|\xi_{-1}\rangle$ ,  $N_{-1}^{\text{th}}/N_{-1}$ , increases with  $t_h$ , where  $N_{-1} = N_{-1}^c + N_{-1}^{\text{th}}$ ,  $N_{-1}^c$ ,  $N_{-1}^{\text{th}}$  are the condensate and thermal components, respectively. At  $t_h = 0.5$  s, the total thermal atom number fraction  $(N_{-1}^{\text{th}} + N_0 + N_1)/(N_{-1} + N_0 + N_1)$  is about 10%. At a given  $t_h$ ,  $N_{0,1}$  is roughly independent of  $\delta$  for  $|\delta|/2\pi \lesssim 1$  kHz, and decreases with increasing  $|\delta|$  [S3]. Besides,  $N_{-1}$  has an exponentially decaying lifetime of 2.7(1) s.

- 
- [S1] H.-R. Chen, K.-Y. Lin, P.-K. Chen, N.-C. Chiu, J.-B. Wang, C.-A. Chen, P.-P. Huang, S.-K. Yip, Y. Kawaguchi, and Y.-J. Lin, *Physical Review Letters* **121**, 113204 (2018).  
[S2] T.-L. Ho, *Physical Review Letters* **81**, 742 (1998).  
[S3] P.-K. Chen, L.-R. Liu, M.-J. Tsai, N.-C. Chiu, Y. Kawaguchi, S.-K. Yip, M.-S. Chang, and Y.-J. Lin, *Physical Review Letters* **121**, 250401 (2018).  
[S4] J. R. Abo-Shaer, C. Raman, J. M. Vogels, and W. Ketterle, *Science* **292**, 476 (2001).  
[S5] R. M. Price, D. Trypogeorgos, D. L. Campbell, A. Putra, A. Valdés-Curiel, and I. B. Spielman, *New Journal of Physics* **18**, 113009 (2016).  
[S6] F. Zambelli and S. Stringari, *Physical Review Letters* **81**, 1754 (1998).  
[S7] Y. Kawaguchi and T. Ohmi, *Phys. Rev. A* **70**, 043610 (2004).